Crack width estimate in reinforced concrete with FBG sensor: experimental and numerical analysis*

WANG Lili, LI Jinghu, HAO Jinguang, SAI Yaozhang, and LIU Xuefeng**
School of Information and Electrical Engineering, Ludong University, Yantai 264025, China

(Received 5 March 2021; Revised 21 June 2021)

A detecting method of investigating the function of crack width versus fiber Bragg grating (FBG) spectrum deformation was proposed. In this paper, the bond-slip model of deformed steel bar in concrete slab was used to calculate the crack width. The stress distributions along optic-fiber grating were extracted by the three-dimensional (3D) finite element method (FEM) and the spectrum deformation of FBG induced by the uneven distribution of the stress was calculated. Experiments were carried out with an FBG fixed on the bottom of concrete slab. The crack width and FBG spectrum deformation of experimental results were given, and the function of crack width versus wavelength shift of FBG sensor was given also. The proposed technology in this paper could improve the safety of large-scale concrete building by early identification of structural crack.
Document code: A **Article ID:** 1673-1905(2022)01-0043-5
DOI https://doi.org/10.1007/s11801-022-1027-8

Recently the health monitoring of large buildings has attracted more and more attention. Strain gauges[1] have been used for such applications and they will continue to provide useful information about structural strains and deformations. The use of embedded fiber Bragg grating (FBG) sensor[2,3] has been a major consideration for damage identification in the field of structural health monitoring (SHM).

Many researchers have investigated the use of embedded FBG sensors for damage detection in composites in real time. In most of these works, the spectrum responses of the fiber Bragg grating based optical sensor were used to obtain quantitative information regarding the crack density[4], crack locations[5], and delamination length[6]. Compared with composite, concrete was a special kind of compound construction material that mainly contains high-quality cements and cementitious ingredients mixed in proper amounts. There were different types of deterioration in concrete structures based on different reasons. KESAVAN[7] analyzed the application of FSOs integrated inside the concrete structures to sense, monitor, and track the overall deterioration and to be able to take appropriate steps. RODRIGUES[8] studied, experimented an FBG-based sensor by applying optical FBG sensing technology embedded in the concrete structured bridges with detailed operation mode. SU[9] studied the bending loss mechanism of optical fiber and presented the monitoring method of hydraulic concrete crack.

Formation of cracks in reinforced concrete structures was a complex phenomenon. The first stage of cracking was induced by shrinkage, corrosive effects and so on. The secondary crack formation was usually resulted from the difference of inextensibility between concrete and steel, and the bonding forces existing between the two. This kind of crack was usually studied by analyzing the model of the loaded reinforced concrete slabs in tension, just as done in this paper. The third stage of cracking[10], always referred to as the equilibrium stage, occurred when no further secondary cracks could be formed, and existing cracks continue to widen.

In this paper, it was assumed that the crack was induced by the deformation difference between rebar and concrete, so the crack width ω was represented by the following equation[11]

$$\omega=\int_0^{l_m}\left(\varepsilon_{sm}-\varepsilon_{cm}\right)dx, \tag{1}$$

where l_m is the crack spacing, and ε_{sm} and ε_{cm} are the strains of rebars and concrete slab in a crack, respectively.

Fig.1 showed the schematic diagram of finite element method (FEM) model. The size of the concrete specimen was 550 mm×150 mm×150 mm. The strength grade of concrete used in experiment was C30. The steel strain gauges fixed on the main rebars were used to measure the steel strains. The FBG stress sensor was fixed on the

* This work has been supported by the National Natural Science Foundation of China (No.61705098), the National Natural Science Foundation of Shandong Province (Nos.ZR2017BF042 and ZR2019MF010), and the Project of Shandong Province Higher Educational Science and Technology Program (No.J17KA050).
** E-mail: wanglili78@hotmail.com

bottom of the concrete beam. The grating length was 8 mm, the core diameter, inner and outer cladding diameter of the grating were 10 μm, 125 μm and 250 μm, respectively. The FBG was packaged by stainless steel tube with length of 100 mm to resist damage induced by external force. The two ends of FBG sensor were fixed on the pouring bolts by universal joints. The maximum wavelength extending of the grating was fixed to less than 4.5 nm to prevent grating breakage.

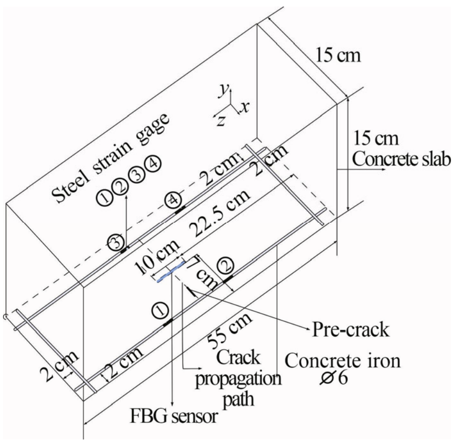

Fig.1 FEM model, including rebars, FBG sensor, strain gages embedded in concrete slab

Another FBG temperature sensor is fixed along the stress sensor for temperature compensation. According to the load direction shown in Fig.2, FBGs were placed along the Z axis shown in Fig.1. As the expected maximum crack width was less than 5 mm, the FBGs were deployed around the middle of the planned crack length. In addition, the FBGs deploy area is at least 2 mm away from the crack propagation path to avoid debonding of the FBGs due to perturbation of the crack propagation.

Fig.2 showed the loading illustrative diagram. The four-point bending test of reinforced concrete slab was implemented through the universal testing machine.

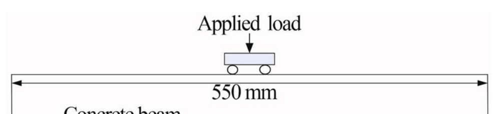

Fig.2 Illustrative diagram of four-point bending test

In the experiment system[12], a quasi-static tensile load was applied to the concrete beam. Tensile load was measured with a load cell and the strain of steel bar was collected by a data acquisition collector which was connected with four steel strain gauges showed in Fig.1. The optical fiber grating was illuminated by a broadband source, whose wavelength range was from 1520 nm to 1570 nm. The reflection spectrum was obtained by using an optical spectrum analyzer (Anritsu MS9740A) while the loading machine was stopped at various values of the tensile load. The wavelength resolution of the optical spectrum analyzer was 0.03 nm.

When the FBG was subjected to service load, various portions of the FBG were under different magnitudes of strain and therefore reflected a wavelength at the corresponding length. The FBG acted as a number of smaller FBGs. This resulted in peak splitting of reflection spectrum[13,14]. Spectral simulations of FBG sensor were implemented based on the transfer matrix formalism[15], in which the grating was divided in to m uniform sub-gratings. $E^+(z)$ and $E^-(z)$ were defined as the slowly varying amplitudes of the forward and backward traveling waves. The propagation through each uniform section was described by a matrix $\boldsymbol{T}^i_{\mathrm{FBG}}$.

$$\begin{bmatrix} E_{i+1}^{+}(z) \\ E_{i+1}^{-}(z) \end{bmatrix} = \boldsymbol{T}^i_{\mathrm{FBG}} \cdot \begin{bmatrix} E_i^{+}(z) \\ E_i^{-}(z) \end{bmatrix} = \begin{bmatrix} T^i_{11} & T^i_{12} \\ T^i_{21} & T^i_{22} \end{bmatrix} \cdot \begin{bmatrix} E_i^{+}(z) \\ E_i^{-}(z) \end{bmatrix}. \tag{2}$$

Once all the matrixes of the individual sections were known, the output amplitudes was obtained as

$$\begin{bmatrix} E_m^{+} \\ E_m^{-} \end{bmatrix} = \boldsymbol{T}^1_{\mathrm{FBG}} \cdot \boldsymbol{T}^2_{\mathrm{FBG}} \cdots\cdots \boldsymbol{T}^m_{\mathrm{FBG}} \begin{bmatrix} E_0^{+} \\ E_0^{-} \end{bmatrix}. \tag{3}$$

To simulate the locally pressed FBG as shown in Fig.1 with this equation, we considered the grating length as the area where the changes of refractive index Δn_{eff} were translated into a shift of the Bragg wavelength $\Delta\lambda_{\mathrm{B}}$. The refractive index changed at any point $M(x, y, z)$ of FBG in the grating zone were given as[12,15,16]:

$$\Delta n_{\mathrm{eff}x}(x,y,z) = -\frac{n_{\mathrm{eff}}^3}{2E}\Big\{(p_{11}-2\nu p_{12})\sigma_x(x,y,z) + \big[(1-\nu)p_{12}-\nu p_{11}\big]\big[\sigma_y(x,y,z)+\sigma_z(x,y,z)\big]\Big\}, \tag{4}$$

$$\Delta n_{\mathrm{eff}y}(x,y,z) = -\frac{n_{\mathrm{eff}}^3}{2E}\Big\{(p_{11}-2\nu p_{12})\sigma_y(x,y,z) + \big[(1-\nu)p_{12}-\nu p_{11}\big]\big[\sigma_x(x,y,z)+\sigma_z(x,y,z)\big]\Big\}, \tag{5}$$

where $n_{\mathrm{eff}x}$ and $n_{\mathrm{eff}y}$ were the effective FBG refractive indices of x-polarization and y-polarization, E and ν were the Young's modulus and the Poisson's coefficient of the optical fiber, p_{11} and p_{12} were the photo-elastic coefficients of the optical fiber, σ_x, σ_y and σ_z obtained from the FEM model were the stress components at any point $M(x, y, z)$ in the FBG in x, y and z directions. The FBG reflection wavelength based on Eqs.(4) and (5) were given as

$$\Delta\lambda_{\mathrm{B}x}(x,y,z) = -\frac{n_{\mathrm{eff}}^3\Lambda_0}{E}\times\Big\{-(p_{11}-2\nu p_{12})\sigma_x(x,y,z) + \big[(1-\nu)p_{12}-\nu p_{11}\big]\big[\sigma_y(x,y,z)+\sigma_z(x,y,z)\big]\Big\} + 2\frac{n_{\mathrm{eff}}\Lambda_0}{E}\Big\{\sigma_z(x,y,z)-\nu\big[\sigma_x(x,y,z)+\sigma_y(x,y,z)\big]\Big\}, \tag{6}$$

$$\Delta\lambda_{\mathrm{B}y}(x,y,z) = -\frac{n_{\mathrm{eff}}^3\Lambda_0}{E}\times\Big\{(p_{11}-2\nu p_{12})\sigma_y(x,y,z) + \big[(1-\nu)p_{12}-\nu p_{11}\big]\big[\sigma_x(x,y,z)+\sigma_z(x,y,z)\big]\Big\} + 2\frac{n_{\mathrm{eff}}\Lambda_0}{E}\Big\{\sigma_z(x,y,z)-\nu\big[\sigma_x(x,y,z)+\sigma_y(x,y,z)\big]\Big\}, \tag{7}$$

where Λ_0 and n_{eff} was the periodicity and refractive parameter of fiber core, respectively.

The mechanical properties of the used materials were all listed in Tabs.1 and 2. In the tables, f_{ck} and f_{tk} were the compression and tensile strength of rebars, ϕ was the rebar diameter, and $\lambda_0=2n_{\mathrm{eff}}\Lambda_0$ was the FBG peak wavelength.The reconstruction of FBG sensor reflective spectrum using transfer matrix method approach was studied with Matlab. The reconstructed FBG reflective spectra at various loads were given in Fig.3(a). The spectra changed remarkably with the variation of strain distributions.

Tab.1 Parameters of concrete slab and rebars used in FEM

	E (GPa)	v	f_{ck} (MPa)	f_{tk} (MPa)	ϕ (mm)
Concrete slab	30	0.2	34.8	3.4	----
Rebars	210	0.3	235	235	8

Tab.2 Parameters of FBG used for the spectrum calculation

λ_0 (μm)	n_{eff}	v	p_{11}	p_{12}
1.55	1.45	0.17	0.121	0.27

The measured reflective spectra of FBG sensor were illustrated at various times. As illustrated in Fig.3(b), the reflective spectrum was symmetrical and had a major peak at the initial stage, and then the measured reflection spectra were distorted significantly with increasing load applied. With the load increasing, the spectra were broadened clearly and the intensity of side lobes increased as well. For the non-uniform distribution, it can be seen that the intensity of side lobes increased asymmetrically with the stress increasing. The experimental results provided a good fitting with the calculated spectra.

The differences between calculated spectra in Fig.3(a) and measured ones in Fig.3(b) were mainly induced by the fact that the stresses extracted from FEM were different from those experimental data. The stresses differences came from the values deviations, such as the compression and tensile strength of concrete slab and rebars, the package of FBG and et al. In addition, the position difference between the FBG sensor in the FEM model and the real embedded positon in the concrete slab would also result in errors. Compared with the measured reflection spectra, the calculated ones had larger wavelength shifts. The calculated peak wavelength was up to 1 556.6 nm whereas the measured one was 1 556.1 nm when the load was 9 kN. However, the calculated results still reproduced the measured spectrum changes, such as the highest peak, spectrum width, and the position of other peaks, very well.

The FBG wavelength shifts and crack width of concrete slab as a function of applied load were shown in Fig.4.

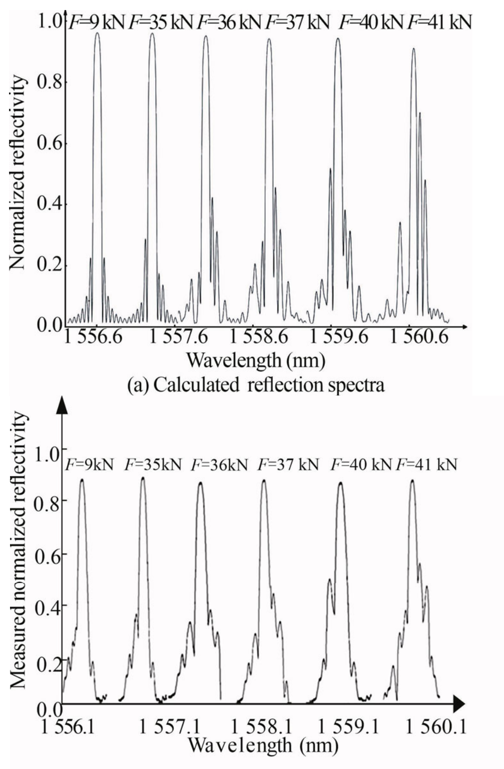

(b) Measured reflection spectra corresponding to the calculated ones

Fig.3 Calculated and measured reflection spectra at various tensile strains of 9 kN, 35 kN, 36 kN, 37 kN, 40 kN and 41 kN, respectively

The parameters of stress and temperature sensors used in experiments were showed in Tab.3. λ_{ε_0} and λ_{T_0} were the initial wavelength of stress and temperature sensors after installation, respectively. K_ε was the displacement coefficient of stress sensor, K_{ε_T} band K_T were the temperature coefficient of stress and temperature sensor, respectively.

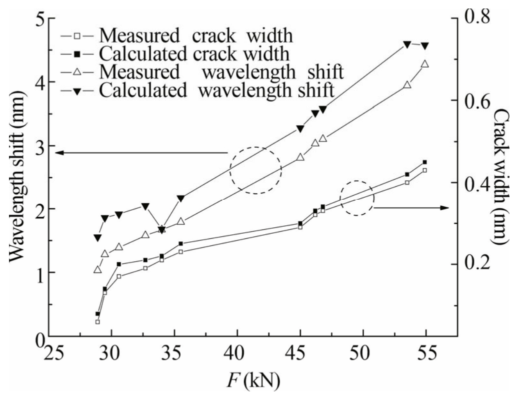

Fig.4 FBG wavelength shifts and crack width of concrete slab as a function of applied load

Tab.3 Parameters of FBG sensors used in experiments

λ_{ε_0} (nm)	λ_{T_0} (nm)	K_ε	K_{ε_T}/K_T
1 555.7	1 535.4	46.59	1

Compared with the theoretical calculation result of 22 kN, the first crack appeared when the applied load was 28.9 kN in the experiment. This difference came from the values deviations, such as the compression and tensile strength of concrete slab and rebar, etc. Fig.4 shows that the measured wavelength shift was 4.9 nm when the load increased to 54.9 kN under which the rebar yielded completely. In fact, other three concrete beams were fatigue loaded during the course of experiment. We found that the FBG broke when load increased to over 55 kN. The variation of crack width with different loads was shown in Fig.6.

By analyzing the experimental results presented in Fig.4, the function of crack width ω versus wavelength shift of FBG stress sensor was given as follows

$$\omega = K_{\varepsilon}\left[\left(\lambda_{\varepsilon}-\lambda_{\varepsilon_0}\right)-\frac{K_{\varepsilon_T}}{K_T}\left(\lambda_T-\lambda_{T_0}\right)\right]. \qquad (8)$$

In addition, by comparing the wavelength shift of FBG sensor and the variation of crack width obtained in experiments, it was demonstrated that the crack test accuracy and test range is up to 0.02 mm and 0.7 mm, respectively.

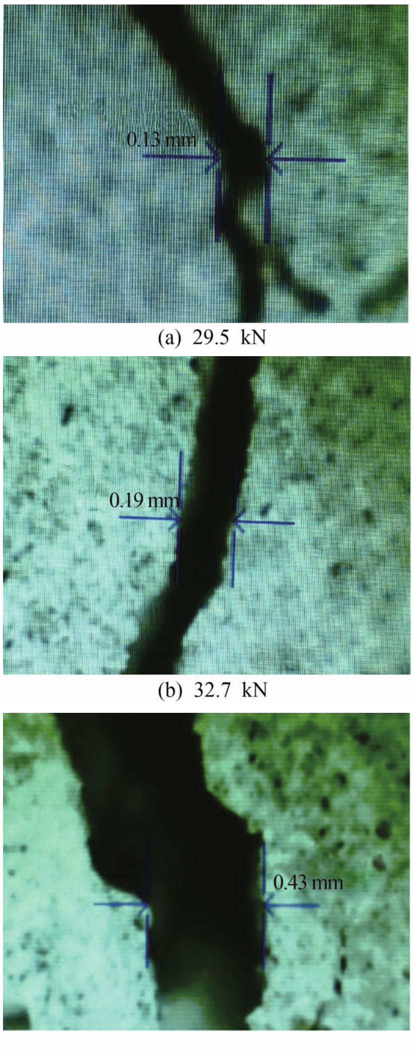

Fig.5 The variation of crack width with different loads

Fig.3 showed the spectrum distortion with an increase of load, we found that 6 dB width of the reflection spectra changed obviously in both the experimental results and the theoretical calculations. The 6 dB spectrum width was defined as the width at a quarter of the reflectivity peak and was plotted as a function of the crack width in Fig.6. Though the calculated spectrum at F=36 kN in Fig.3(a) was still narrow and had only one reflectivity peak, whereas the measured 6 dB spectrum width was much larger as shown in Fig.3(b). Besides the influence of the parameters deviation between the FEM and experimental test, this was partly induced by the residual stresses applied to the FBG sensor during the curing process. Fig.6 showed that the 6 dB spectrum width increased consistently with the crack width and it was found that the crack width could be evaluated reliably depending on the spectrum width in general.

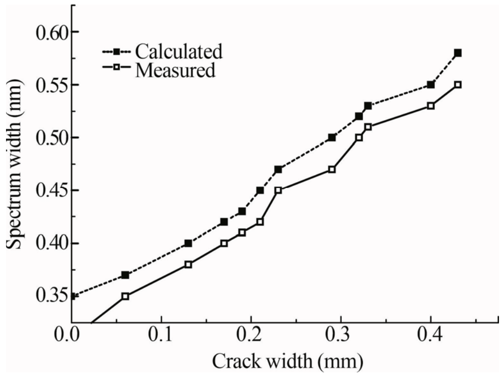

Fig.6 Relationship between the spectrum width and the crack width

Fig.3 also showed that the side mode intensity varied with the increasing load. Like the central wavelength shifts showed in Fig.4, the intensity ratio of the peak mode to the secondary one was recorded as the reference, the ratio versus crack width was used as the damage index as shown in Fig.7. The solid and the dashed lines were the measured and calculated results respectively. The results showed that the intensity ratio of FBG sensor changed significantly with crack widening. This phenomenon should be caused by the stress distribution that varied with different crack width. The results showed the calculated and the measured spectra had the same tendency. The error between the calculated and the experimental results was that the positional and parametric deviation of the FBG sensor in the FEM model from the real one in the experimental specimen.

To further illustrate the reliability of 8-mm-long FBG sensor under tensile load experiments, the spectra of FBG sensors were recorded with different experiment specimen. One may note that the FBG sensor holds its integrity for the entire duration of the test and does not show any noticeable degradation, which clearly points out the reliability and accuracy of the measurement.

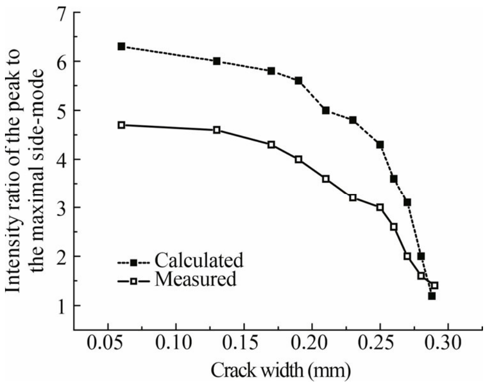

Fig.7 Ratio of the maximal side-mode to peak intensity changes versus crack width

An approach was presented to implement the crack detection in concreted structure based on the reflection behavior of FBG sensor. With regard to the application of this technique for practical use, there exist some issues. The FBG sensors could detect only one transverse cracks around the sensors. If there were two or more transverse cracks, the combined action of multiple cracks would also cause the peak wavelength shift, the spectrum width widening and the ratio increase of the peak mode to the secondary one. So the load should be able to make the crack extend along the direction of the pre-crack to ensure the reliability and accuracy of the measurement.

Statements and Declarations

The authors declare that there are no conflicts of interest related to this article.

References

[1] KAKLAUSKAS G, SOKOLOV A, RAMANAUSKAS R, et al. Reinforcement strains in reinforced concrete tensile members recorded by strain gauges and FBG sensors：experimental and numerical analysis[J]. Sensors (Basel), 2019, 19(1)：200.

[2] LIU Y G, YANG D Q, WANG Y X, et al. Fabrication of dual-parameter fiber-optic sensor by cascading FBG with FPI for simultaneous measurement of temperature and gas pressure[J]. Optics communications, 2019, 443：166-171.

[3] DATTA A, BABU A M, SAHA A. Enhanced sensitivity of fiber optic evanescent wave absorption-based concentration sensor by shining a Bessel-Gauss beam and effect of fiber bending on the sensor response：a theoretical analysis[J]. Optical engineering, 2019, 58(5)：1-12.

[4] OKABE Y, YASHIRO S, KOSAKA T, et al. Detection of transverse cracks in CFRP composites using embedded fiber Bragg grating sensors[J]. Smart material structure, 2000, 9(6)：832-838.

[5] OKABE Y, TSUJI R, TAKEDA N. Application of chirped fiber Bragg grating sensors for identification of crack locations in composites[J]. Composites part A-applied science and manufacturing, 2004, 35(1)：59-65.

[6] TAKEDA S, OKABE Y, TAKEDA N. Delamination detection in CFRP laminates with embedded small-diameter fiber Bragg grating sensors[J]. Composites part A-applied science and manufacturing, 2002, 33(7)：971-980.

[7] KESAVAN K, RAVISANKAR K, PARIVALLAL S, et al. Experimental studies on fiber optic sensors embedded in concrete[J]. Measurement, 2010, 43(2)：157-163.

[8] RODRIGUES C, FÉLIX C, LAGE A, et al. Development of a long-term monitoring system based on FBG sensors applied to concrete bridges[J]. Engineering structure, 2010, 32(8)：1993-2002.

[9] SU H Z, LI X, FANG B, et al. Crack detection in hydraulic concrete structures using bending loss data of optical fiber[J]. Journal of intelligent material systems and structures, 2017, 28(13)：1719-1733.

[10] DAWOOD N, MARZOUK H. Crack spacing and width of thick high strength reinforced concrete panels[J]. Advances in structural engineering, 2013, 16(2)：273-285.

[11] SOLTANI A, HARRIES K A, SHAHROOZ B M. Crack opening behavior of concrete reinforced with high strength reinforcing steel[J]. International journal of concrete structures and materials, 2013, 7(4)：253.

[12] WANG L L, HAO J G, SAI Y Z. Crack opening estimate of reinforced concrete using optical fiber sensor[C]//2020 IEEE 5th Optoelectronics Global Conference, September 7-11, 2020, Shenzhen, China. New York：IEEE, 2020：137-139.

[13] GAFSI R, EL-SHERIF M A. Analysis of induced birefringence effects on fiber Bragg gratings[J]. Optical fiber technology, 2000, 6(3)：299-323.

[14] WANG L L, XIN X J, SONG J, et al. Finite element analysis-based study of fiber Bragg grating sensor for cracks detection in reinforced concrete[J]. Optical engineering, 2018, 57(2)：1-6.

[15] ERDOGAN T. Fiber grating spectra[J]. Journal of lightwave technology, 1997, 15(8)：1277-1294.

[16] WANG L L, SONG J, SAI Y Z, et al. Crack width analysis of reinforced concrete using FBG sensor[J]. IEEE photonics journal, 2019, 11(1)：1-8.